Chinese Chemical Letters 34 (2023) 108190

Contents lists available at ScienceDirect

Chinese Chemical Letters

journal homepage: www.elsevier.com/locate/cclet

Iron atom–nanoparticles for interactional enhancing the electrocatalytic reaction activity in Li-S batteries

Gamal H. Al-Shawesh[a,b], Jiawen Zhu[a], Wei Zhang[a], Shuai Xie[a], Junjie Xu[c], Guolei Cai[a], Amar Y. Al-Ansi[a], Yunhong Wei[a,*], Song Jin[a], Hengxing Ji[a,*]

[a] Hefei National Laboratory for Physical Sciences at the Microscale, CAS Key Laboratory of Materials for Energy Conversion, Department of Applied Chemistry, University of Science and Technology of China, Hefei 230026, China
[b] Department of Chemistry, Faculty of Education, Thamar University, Dhamar, Yemen
[c] School of Chemistry and Chemical Engineering, Hefei University of Technology, Hefei 230009, China

ARTICLE INFO

Article history:
Received 7 November 2022
Revised 15 December 2022
Accepted 2 February 2023
Available online 6 February 2023

Keywords:
N-doped carbon nanotubes
Iron atoms
Iron nanoparticles
Electrocatalyst
Li-S batteries

ABSTRACT

The undesirable shuttle effect and sluggish redox kinetics of polysulfides seriously result in low sulfur utilization and poor capacity retention. Here, an integrated strategy is proposed by rational designing multifunctional architecture to manipulate the redox kinetics of polysulfides, specifically, by employing iron atoms (Fe-As) and iron-species nanoparticles (Fe-NPs) co-embedded nitrogen-doped carbon nanotube (Fe-NCNT) as catalyst and host for sulfur. The synergistic cooperation of Fe-As and Fe-NPs provides efficient active sites to facilitate the diffusion, strengthen the affinities, and promote the conversion reactions for polysulfides. Furthermore, the NCNT not only offers practical Li^+ transport pathways but also immobilize the polysulfides effectively. Benefiting from these merits, the Fe-NCNT/S electrodes exhibit high initial specific capacity of 1502.6 mAh/g at 0.1 C, outstanding rate performance (830 mAh/g at 2 C), and good cycling performance (597.8 mAh/g after 500 cycles with an ultralow capacity fading rate of 0.069% per cycle). This work features the distinct interaction of iron atom-nanoparticles on facilitating immobilization-diffusion-transformation process of polysulfides, and it also expected to pave the way for the application in practical Li-S batteries.

Lithium-sulfur (Li-S) batteries are regard as one of the most promising energy storage devices owing to its extremely high theoretical specific capacity of 1675 mAh/g, satisfactory theoretical energy density of 2600 Wh/kg, and environment friendly features [1,2]. However, Li-S battery is still hindered by several issues, that need to be addressed to realize their practical application, including: (1) Severe shuttle effect of lithium polysulfides (Li_2S_x, $4 \le x \le 8$), resulting in low Coulombic efficiency and rapid capacity decay during cycling [3–5]; (2) Sluggish redox kinetics [6], leading to incomplete reveres conversions between S_8, Li_2S_x and Li_2S_2/Li_2S [7]; (3) Low sulfur utilization, resulting from the poor conductivity of sulfur and insoluble sulfides.

To overcome these above problems, tremendous efforts have been devoted to combating the polysulfides shuttling effect using three main strategies, specifically, physical confinement, chemical adsorption, and electrocatalysis. Most of the pervious works focused on designing graphene, carbon nanotubes (CNTs) [8–11], porous hollow carbon structures [12], and polymer/biomass derived carbon [13] as sulfur host materials. Most of these materials have abundant pores or interlayer spaces to physically or electrostatically trap the polysulfides, while the weak interaction between the nonpolar carbon materials and polar polysulfides cannot suppress the shuttle effect completely, resulting in the severe decay of capacity and poor rate capability. Therefore, by introducing polar materials into carbon materials arouses the interests because it could provide the capability of chemical adsorption for polysulfides species. Among the polar materials, metal oxide (*e.g.*, TiO_2, Fe_2O_3, Co_3O_4 and ZnO) [14–17], metal nitride (VN, TiN, InN and CoN) [18–21], metal sulfide (CoS_2, ZnS and VS) [22–24], and bimetallic alloys (Co_xSn_y) [25] are widely reported owing to its strong interaction ability with polysulfides, which can enhance the redox reaction kinetics, mitigate the shuttle effect, and boost the capacity retention for Li-S batteries [26]. Moreover, some of the metal compound also showing the electrocatalysis property to help the sulfur species reacts efficiently and accelerate the conversion of polysulfides [27]. To date, the catalysts with well active sites and satisfied adsorption ability have verified to be effective in enhancing the reaction kinetics. Although these strategies have made significant progress

---

* Corresponding authors.
E-mail addresses: weiyunhong@ustc.edu.cn (Y. Wei), jihengx@ustc.edu.cn (H. Ji).

https://doi.org/10.1016/j.cclet.2023.108190

in improving the electrochemical performance of Li-S batteries, the results have not yet reached the required level. To further eliminate the shuttle effect, a fundamental breakthrough is still required.

Engineering of single-atom catalysts for enhancing polysulfides conversion has been also put forward in Li-S batteries due to their large surface coverage and homogeneous structures. The individual catalytic sites with unsaturated metal coordination are enable facilitate electron transfer and redox reactions in batteries [28,29]. Therefore, introduction of heterogeneous metal atoms (Fe, Co and Ni) or non-metal-atoms (N, P, S and B) into the carbon matrix has been proved as an effective strategy for high-performance Li-S batteries. For instance, Wan's group reported that the Co atoms diffused in N/G and formed a stable coordination center (Co−N/G) as bifunctional electrocatalysts can accelerate the conversion of polysulfides. Thus, the S@Co−N/G composite delivered a high specific capacity of 1210 mAh/g and maintained a discharge capacity of 681 mAh/g after 500 cycles [30]. Among them, iron series metal atom-decorated carbon materials as catalyst for Li-S batteries attracts the attention of researchers because they are distinguished not only by their high catalytic ability, but also by their characters of natural abundance, low-cost, and non-toxicity. Yang *et al.* reported that the hybrid structure of single iron and porous nitrogen-doped carbon as catalysts can enhance the kinetics of polysulfides conversion in Li-S battery. The hybrid structure exhibited high cycling stability of 557.4 mAh/g at 0.5 C over 300 cycles with Columbic efficiency of 99.0% and capacity decay 0.2% per cycle, which ascribed to the strong interaction of Fe with polysulfides and physical adsorption on the micro-mesoporous carbon [31]. Single-atomic iron catalysts play a significant role in inhibiting the intermediate dissolved polysulfides and improving the kinetics of the polysulfide conversion reaction [32]. However, there are very few literatures regarding the attempts of iron atom–nanoparticles composite catalysts to interactional increase the electrocatalytic sulfur reduction reaction activity in Li-S batteries.

Taking the above into consideration, herein, we report a novel composite architecture with iron atoms (Fe-As) and iron-species nanoparticles (Fe-NPs) embedded nitrogen-doped carbon nanotube (Fe-NCNT) catalyst for sulfur cathode. The Fe-NCNT catalyst rapidly converts polysulfides to the insoluble Li_2S during the discharge process and catalytically oxidizes Li_2S back into S_8 during the charge process. The homogeneous distribution of Fe-As and Fe-NPs on the NCNT provide efficient active sites to suppress the shuttle effect of polysulfides through strong chemical interactions and promoted polysulfides conversion. Furthermore, the NCNT not only offers practical Li^+ transport pathways but also exposes the Fe species sites for catalyzing polysulfide conversion. Due to the aforementioned synergistic effect, the Fe-NCNT/S cathode with sulfur content of 70 wt% provided a high initial specific discharge capacity of 1502.6 mAh/g at 0.1 C and stable cycling life (a low capacity decay of 0.069% per cycle at 1 C over 500 cycles). Besides, a remarkable high-rate capacity of 830 mAh/g at 2 C and high capacity retention of 78.7% when the current density switches back to 0.2 C are also achieved for Fe-NCNT/S.

The Fe-NCNT catalyst was prepared by pyrolyzing of Fe-ZIF-8 with introduction of ethanol, as shown in Fig. S1 (Supporting information). The introduction of ethanol at high temperature dissociates and generates hydroxyl radical, which reacts with the neighboring carbon atoms to produce carbon monoxide, facilitating the removal of the amorphous carbon, leading to the improved electrical conductivity of the carbon nanotube. Besides, Fe-As and Fe-NPs are obtained along with a large number of porous carbon nanotubes generated. The morphology and microstructure of Fe-NCNT were probed by scanning electron microscopy (SEM) and transmission electron microscopy (TEM) images (Figs. 1a-c). The as-prepared Fe-NCNT shows a porous fiber network with uniform diameter of 50–100 nm as well as a large number of internal voids. Besides, some tiny nanoparticles with a diameter of 20–50 nm are confined in the porous canal of the fiber matrix. To further demonstrate the existence of Fe-NPs, high-resolution TEM (HRTEM) image is further substantially proved. As shown in Fig. 1d, the lattice fringes with spacing of 0.21 nm are corresponding to the (111) plane of FeN or the (211) plane of Fe_3C. In addition, a distinct lattice distance of around 0.35 nm that corresponds to (002) plane of the sp^2 carbon, which is mainly synthesized with catalysis by Fe species. To further confirm the presence and distribution of Fe-As in NCNT, atomic-resolution high-angle annular dark-field scanning TEM (HAADF-STEM) was performed. As shown in Figs. 1e and f, the Fe-As (bright small dots) are randomly dispersed and anchored on NCNTs matrix, indicating that the atomic sites of Fe were formed, as well the coexistence of Fe-As and Fe-NPs on the NCNT is observed. Additionally, Fig. 1e also clearly depicts a cluster nanopore (yellow circle) surrounded by Fe-As (blue circles) that allows rapid transfer of electrons. Besides, the HAADF-STEM coupled with EDX element mapping results further confirms the dispersion of Fe and N homogeneously on the carbon matrix (Fig. 1g). The presence of Fe species induces catalyzing the growth of carbon nanotube and enhances the graphitization degree of Fe-NCNT. To verify this, the sample prepared by treating Fe-NCNT with HCl (named as rFe-NCNT) and commercial NCNT are adopted for comparison.

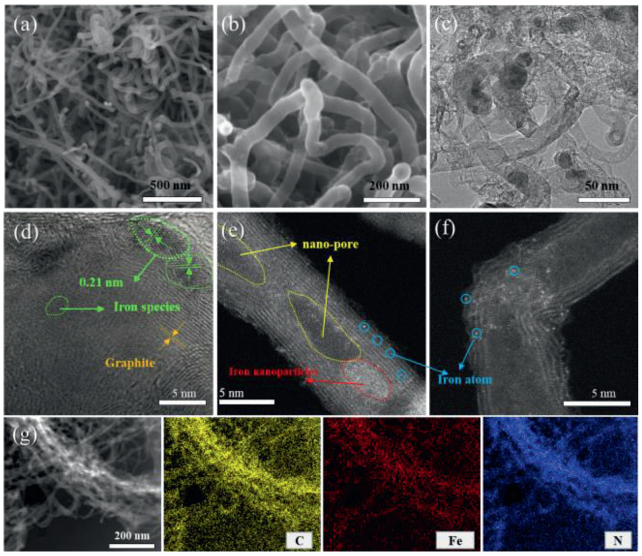

Fig. 1. Morphological characterization of Fe-NCNT. (a, b) SEM images of Fe-NCNT. (c) TEM image and (d) HRTEM image of Fe-NCNT. (e-g) HAADF-STEM image and the corresponding EDX element distribution of Fe-NCNT.

The crystallographic structures of Fe-NCNT and rFe-NCNT were studied by X-ray diffraction (XRD). As shown in Fig. 2a, the diffraction sharp peak at 26.4° are belong to (002) plane of graphite, indicating that the carbonaceous structure is produced with a high degree of graphitization. Moreover, the diffraction peaks at 43.6° and 50.8° are attributed to the (111) and (200) planes of $FeN_{0.0324}$ (JCPDS No. 75–2127). And the diffraction peaks at 42.9°, 43.7° and 45.0° are corresponding to the (211), (102) and (031) planes of Fe_3C (JCPDS No. 35–0772). However, the diffraction peaks at 44.6° and 65.0° corresponding to the (110) and (200) planes of Fe (JCPDS No. 06–0696) are disappeared when treating Fe-NCNT with HCl, illustrating that most of the Fe-NPs have been removed after treatment with a high concentration of acid, which is further evidenced by TEM. As shown in Fig. S2 (Supporting information), the TEM images show typical tube morphologies of rFe-NCNT after removal of Fe-NPs outside of NCNTs, while only numerous opened tubes with diameter of about 5 nm can be observed, demonstrating that most of the Fe-NPs can be removed. Raman spectra of Fe-NCNT, rFe-

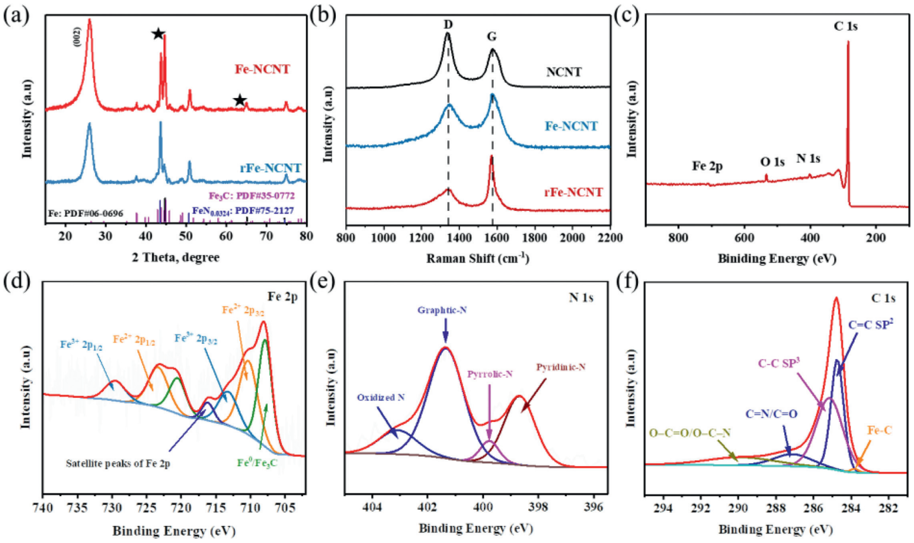

Fig. 2. (a) XRD pattern and (b) Raman spectra of Fe-NCNT, rFe-NCNT and NCNT. (c) XPS survey spectra and high-resolution XPS spectra of (d) Fe 2p, (e) N 1s, and (f) C 1s in Fe-NCNT.

NCNT, and NCNT are shown in Fig. 2b. We observed that the three samples contained two obvious and prominent peaks at around 1569.5 cm^{-1} and 1341.4 cm^{-1}, which are ascribed to the D band (corresponding to the lattice defects of defective/disordered sp^3 hybridized carbon) and G band (representing the distinctive peak of sp^2 structure), respectively [33]. The relative intensities ratio of I_G/I_D for Fe-NCNT is 2.82, much higher than that of rFe-NCNT (1.35) and NCNT (0.72). Such a high graphitization degree achieved by Fe-NCNT could lead to improved electrical conductivity for rapid electron transfer in lithium-sulfur batteries [34]. The removal of the Fe-NPs from Fe-NCNT could lead to a defect in the carbon nanotube lattice, thus leading to a decrease in the graphitization degree of rFe-NCNT.

X-ray photoelectron spectroscopy (XPS) measurements were used to confirm the surface composition and chemical bonding state of Fe-NCNT. The XPS survey spectra of Fe-NCNT provided direct evidence of the existence of carbon, nitrogen, oxygen, and iron elements (Fig. 2c). The total content of N, O and Fe are around 1.8 wt%, 2.3 wt% and 1.3 wt%, respectively, where the percent of Fe in Fe-NCNT is confirmed by ICP test. The high-resolution XPS spectra of Fe 2p is shown in Fig. 2d. The binding energies at 707.9 eV and 720.8 eV can be related to Fe-C bonding or zero-valence metallic Fe. In addition, the other two pairs of peaks with binding energies of 710.23/723.48 eV and 713.3/729.7 eV can be assigned to the Fe-O (Fe^{2+}) and Fe-O (Fe^{3+}), respectively. The existence of Fe-O bonds is mainly attributed to the inevitable oxidation of the air-exposed Fe-NPs during the XPS test [35,36]. For the high-resolution N 1s spectrum (Fig. 2e), the peaks located at 398.6, 399.8 and 401 eV are indexed to pyridinic N, pyrrolic-N, and graphitic N, respectively. The existence of pyridinic N in NCNT is identified as carrier, which possessing quite a lot of active sites for enhancing the chemisorption of LiPS. Furthermore, graphitic N can increase the electrochemical conductivity owing to the C–N bonds can induce an inhomogeneous distribution of electrons [37,38]. The C 1s spectrum further confirms the presence of the carbon-functional groups. As shown in Fig. 2f, the C 1s spectrum are deconvoluted into four distinct peaks as follows: Fe-C (283.7 eV), sp^2 C=C (284.8 eV), C–C sp^3 (285.6 eV), and C=O/C=N (287.4 eV). There is a strong correlation between the C–C peak and the sp^2 hybridization of carbon atoms. The existence of C–N bond indicates that N has been successfully incorporated into the carbon matrix. The peak located at 287.4 eV are associated with surface oxygen and nitrogen group, which originated due to the oxygen absorbed on the surface from the surrounding environment [39]. The nitrogen adsorption/desorption isotherms measurements were used to verify the specific surface area and the combined pore structures. As shown in Fig. S3 (Supporting Information), the as-prepared Fe-NCNT and rFe-NCNT exhibit a distinctive type-IV isotherm with hysteresis loops, which confirms that the microporous and mesoporous channels coexist in the materials. The Brunauer–Emmett–Teller (BET) specific surface area of Fe-NCNT and rFe-NCNT were calculated to be 138.15 and 181 m^2/g, respectively. As predicted, rFe-NCNT also exhibited a larger pore volume (0.601 cm^3/g) compared with Fe-NCNT (0.672 cm^3/g), which were calculated by Barrett–Joyner–Halenda (BJH) methods. The relatively larger specific BET surface area and pore volume of rFe-NCNT were attributed to the removal of Fe-NPs.

In order to evaluate the practicality of Fe-NCNT as sulfur hosts, sulfur was infiltrated into Fe-NCNT by a conventional melt-diffusion method. The corresponding XRD pattern of resultant Fe-NCNT/S and rFe-NCNT/S composites reveal an orthorhombic S_8 structure, demonstrating that a considerable quantity of sulfur was successfully loaded into both samples (Fig. S4a in Supporting information). Thermogravimetric analysis (TGA) was conducted to investigate the content of sulfur in the Fe-NCNT/S and rFe-NCNT/S composites under N_2 atmosphere. As shown in Fig. S4b (Supporting information), the sulfur content in both two composites is around 70%. The morphology of Fe-NCNT/S and rFe-NCNT/S are showing in Fig. S5 (Supporting information). The SEM images show that no visible aggregate S particles can be found on the surface of the two samples, suggesting the excellent infiltration of sulfur into the porous carbon matrix.

The electrocatalytic performance for the as-prepared Fe-NCNT/S, rFe-NCNT/S, and NCNT/S cathode were investigated paired with Li foil as anode in Li-S batteries. The cyclic voltammogram (CV) confirmed the accelerated polysulfide redox reaction of Fe-NCNT/S cathode in Li-S batteries. As depicted in Fig. 3a, two reduction cathodic peaks at 2.24 and 2 V are obtained which correspond to the reduction of S_8 to soluble polysulfides (Li_2S_8, Li_2S_6 and Li_2S_4), and then these polysulfides further convert to insoluble Li_2S_2/Li_2S. Compared with the rFe-NCNT/S electrode, the Fe-NCNT/S electrode delivers a smaller potential deviation, indicating that the Fe-NCNT possess the higher ability to accelerate the redox reaction kinetic effectively. Besides, one anodic peak for Fe-NCNT/S and rFe-NCNT/S composites is noticeable at 2.43 V, which may be

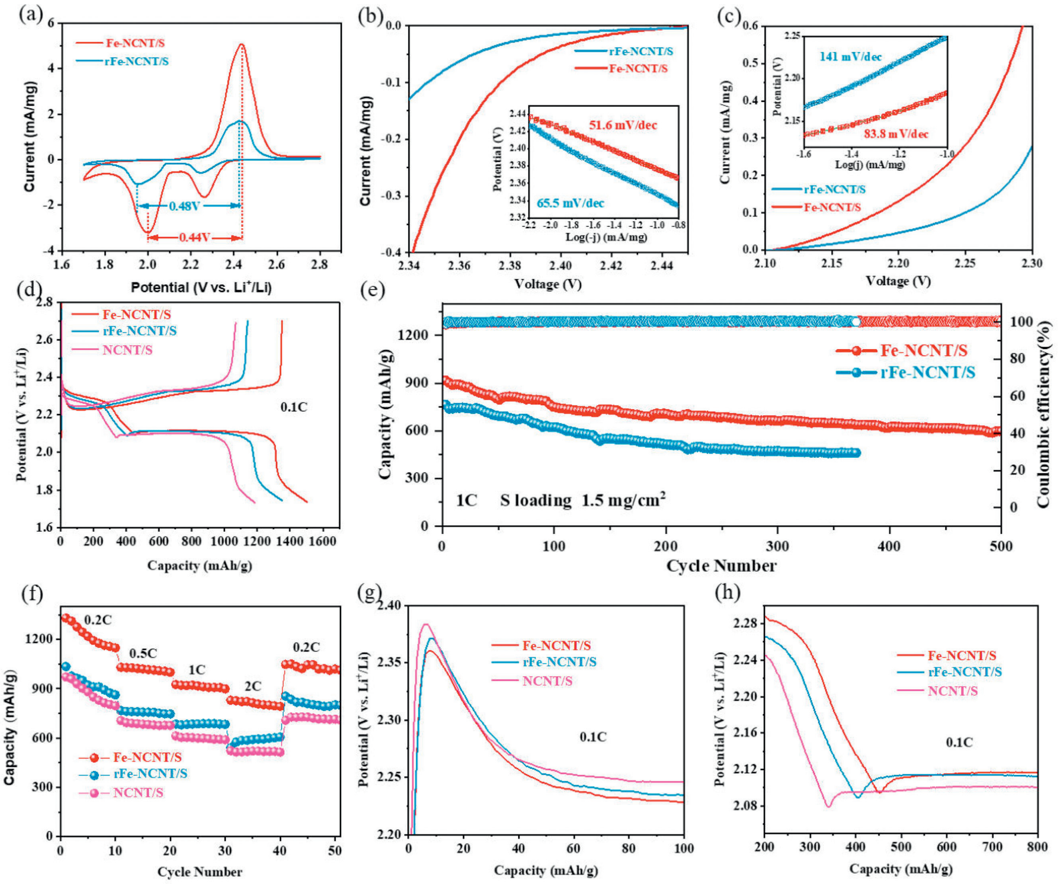

Fig. 3. Electrochemical performance of Fe-NCNT/S, rFe-NCNT/S, and NCNT/S cathodes. (a) CV curves of Fe-NCNT/S and rFe-NCNT/S cathodes at a scan rate of 0.2 mV/s between 1.7 V and 2.8 V. Tafel plots of initial (b) reduction and (c) oxidation processes. (d) The first galvanostatic charge–discharge curves at 0.1 C. (e) Long-term cycle performance at 1 C. (f) Rate performance for Fe-NCNT/S, rFe-NCNT/S and NCNT/S at various current densities. (g, h) The initial charge-discharge profiles of Fe-NCNT/S, rFe-NCNT/S and NCNT/S at 0.1 C.

ascribed to the oxidation of Li_2S_2/Li_2S to S_8. In brief, the higher peak intensities and smaller potential deviation of Fe-NCNT/S electrode indicates the significantly improved redox kinetics of polysulfides.

To further analyze the catalytic activity of Fe-NCNT, Tafel slopes are calculated and compared by the CV curves, as shown in Figs. 3b and c. The calculated Tafel slopes of the initial reduction and oxidation processes are 51.6 and 83.8 mV/dec for the Fe-NCNT/S electrode respectively, obviously smaller than the rFe-NCNT/S electrode (65.5 and 141 mV/dec), indicating the enhanced catalytic effect of Fe-NPs on dynamically accelerating the Li–S redox kinetics. The synergistic effect between the polar iron species and the outstanding conductivity of Fe-NCNT contributed to improving the adsorption ability for polysulfides and enhancing the utilization efficiency of sulfur. Therefore, compared with rFe-NCNT/S and NCNT/S electrodes (1351.6 mAh/g and 1181 mAh/g), respectively, the Fe-NCNT/S electrode exhibits a smaller polarization and higher initial specific discharge capacities (1502.6 mAh/g), as exhibited in Fig. 3d. The cycling performance of Fe-NCNT/S and rFe-NCNT/S electrode displayed in Fig. 3e. Owing to the outstanding catalytic capability and polysulfide confinement of Fe-NCNT, the Fe-NCNT/S electrode revealed good cycling stability of 596.9 mAh/g at 1 C after 500 cycles, with almost 99.9% of Columbic efficiency and 0.069% of the capacity decay per cycle, much lower than that of rFe-NCNT/S electrode (0.11% per cycle) with the same sulfur loading of 1.5 mg/cm^2. Moreover, the Fe-NCNT/S electrode with mass loading of 2.3 mg/cm^2 also delivered a high discharge capacity of 945 mAh/g at 0.5 C current density, and the capacity still maintains 610.6 mAh/g after 200 cycles (Fig. S6 in Supporting information). Even improving the sulfur loading to 4.5 mg/cm^2 with the E/S ratio of 10 µL/mg, a considerable initial capacity as high as 943 mAh/g is able to still achieve at 0.2 C, and it can maintain stably for 60 cycles (Fig. S7 in Supporting information). These results imply that the dual synergistic effect of chemisorption and electrocatalysis of Fe-NCNT catalyst can effectively inhibit the shuttle effect and improve the cycle stability. Table S1 (Supporting information) displays comparison of the electrochemical performance of Fe-NCNT with previously studied Fe-based cathode hosts for Li-S batteries.

The galvanostatic charge/discharge measurements further confirmed the electrochemical performance at different current densities of the Fe-NCNT/S, rFe-NCNT/S and NCNT/S electrodes (Fig. 3f). The Fe-NCNT/S electrode exhibited a high specific capacity of 1330.4, 1030.4, 925.5, and 829.9 mAh/g at 0.2, 0.5, 1 and 2 C, respectively, while the rFe-NCNT/S electrode delivered 1034.79 mAh/g at 0.2 C and 606.4 mAh/g at 2 C. In compression, the NCNT/S just delivered 971.6 mAh/g at 0.2 C and 522.8 mAh/g at 2 C. When the current density switch back to 0.2 C, the specific discharge capacity of Fe-NCNT/S electrode can still maintain 1047.3 mAh/g with a high retention rate of 78.7%, indicating that the Fe-NCNT/S electrode has good reversibility and enhanced sulfur utilization. More importantly, the Fe-NCNT/S shows a smaller voltage hysteresis over the rFe-NCNT/S at different current densities (Fig. S8 in Supporting information). The polarization voltage gaps of Fe-NCNT/S and rFe-NCNT/S increase with the increase of the current densities from 0.1 C to 2 C. Even so, the Fe-NCNT/S composite showed the lowest polarization voltage gap of 219.5 mV at the cur-

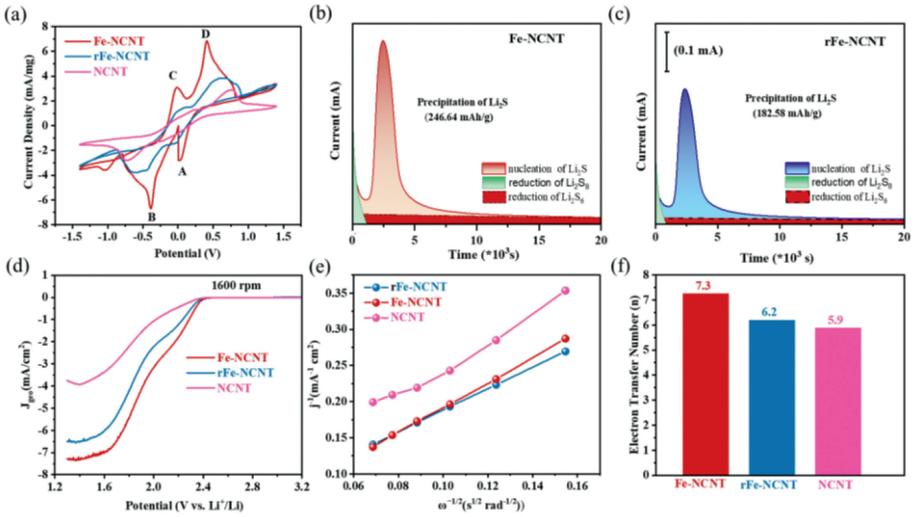

Fig. 4. Electrocatalytic effect of Fe-NCNT, rFe-NCNT and NCNT on LiPSs conversion. (a) The CV curves of symmetrical cells based on Fe-NCNT, rFe-NCNT, and NCNT electrodes immersed in the electrolyte containing 0.5 mol/L Li_2S_6. (b, c) Chronoamperometry curves of Fe-NCNT, rFe-NCNT and NCNT in Li_2S_8/tetraglyme solution at 2.06 V. (d) RDE measurement for Fe-NCNT, rFe-NCNT and NCNT at 1600 rpm. (e) Koutecky–Levich equation plot of J^{-1} *versus* $\omega^{-1/2}$. (f) An electron transfer number comparison among Fe-NCNT, rFe-NCNT and NCNT.

rent density of 0.2 C and 479.3 mV at the current density of 2 C. Compared with rFe-NCNT/S (420 mV), the increase in the voltage gap of Fe-NCNT/S from 0.1 C to 2 C is only 262.6 mV due to the improved catalytic activity of the Fe-NCNT catalyst. To further confirm the catalytic ability of Fe-NCNT, the potential barrier of the charge/discharge processes was conducted at 0.1 C. Fig. 3g displays the first part of the charge plateaus, in which the overpotentials for the conversion of insoluble Li_2S/Li_2S_2 to soluble polysulfides can be reflected by the positive potential peak at the outset of the initial charge plateaus. While the first discharge plateaus in Fig. 3h represents the overpotential at which soluble Li_2S_4 is converted to insoluble Li_2S_2. It is obvious that cell with Fe-NCNT/S shows the lowest overpotentials in both the charge and discharge profiles, which is corresponding with the enhanced redox reaction kinetics of LiPSs on Fe-NCNT (Fig. 4a). This could be attributable to the synergistic cooperation of Fe-As and Fe-NPs species on the NCNT, which provides efficient active sites to suppress the shuttle effect of polysulfides through strong chemical interactions and promoted polysulfides conversion. The adsorption ability of polysulfides for Fe-NCNT was further confirmed by visualized polysulfides adsorption tests combined with UV–vis adsorption spectra. As exhibited in Fig. S9 (Supporting information), the solution adsorbed by Fe-NCNT is clear and transparent after 12 h. Besides, the Fe-NCNT also exhibited a substantially lower polysulfides peak intensity compared to rFe-NCNT and NCNT, indicates that Fe-NCNT is more capable of adsorbing polysulfides, that is, the presence of Fe-species plays a role in the adsorption of polysulfides.

To further evaluate the electrocatalytic activity of Fe-NCNT symmetric cells were assembled using rFe-NCNT and NCNT as comparison. Fig. 4a shows the CV curves of Fe-NCNT, rFe-NCNT, and NCNT electrodes, which performed within a potential window from −1.4 V to 1.4 V using Li_2S_6 electrolyte. The CV curve for Fe-NCNT electrode exhibits two pairs of obvious reduction peaks and oxidation peaks at 0.018 V/−0.38 V and −0.013 V/0.41 V, respectively, labeled as A, B, C and D. By comparison, the presence of Fe-As and Fe-NPs renders sharper redox peaks, higher current density, and lower voltage hysteresis between the anodic and cathodic peaks for the Fe-NCNT electrode over the rFe-NCNT, and NCNT electrodes. All these indicate that the polysulfide redox reaction kinetics and the reversibility greatly enhanced with the presence of Fe-As and Fe-NPs species decorated in NCNT architecture. It suggests that the Fe-NCNT electrode could offer more catalytic sites and efficiently accelerate the electrochemical polysulfide redox reactions, leading to lower polarization and higher electrochemical reversibility. Specifically, Fig. S10 (Supporting information) shows the potential and current density of peak D. Compared with rFe-NNCT and NCNT electrodes, the Fe-NCNT electrode exhibited the highest current density of 6.8 mA and the lowest potential of 0.4 V, indicating that the kinetics of polysulfides conversion on the Fe-NCNT electrode is faster than that on rFe-NCNT and NCNT, and the energy barrier of the Fe-NCNT electrode is lower than that in rFe-NCNT and NCNT electrode.

The precipitation of Li_2S experiment was conducted to verify the deposition performance of Li_2S precipitation on Fe-NCNT catalyst by utilizing Li_2S_8/tetraglyme solution as electrolyte. Figs. 4b and c and Fig. S11 (Supporting information) illustrate the nucleation and growth of Li_2S for Fe-NCNT, rFe-NCNT and NCNT electrodes, respectively. The potentiostatic discharge experiments accurately describe the reduction process of Li_2S_8/Li_2S_6, as well as the precipitation of Li_2S. According to the calculations, the quantity of Li_2S precipitation on Fe-NCNT, rFe-NCNT, and NCNT are calculated to be 246.63, 182.58 and 119.13 mAh/g, respectively. The higher Li_2S precipitation capacity for Fe-NCNT indicates that most of the polysulfides participated in the reduction reaction instead of dissolving in the electrolyte and going to the anode side through the separator, thus leading to superior electrocatalytic activity over rFe-NCNT and NCNT. To confirm this point, we further conducted CV scans on a rotating disk electrode (RDE) measurement. As shown in Fig. 4d, the current density of Fe-NCNT at 1600 rpm is higher than rFe-NCNT and NCNT, indicating that the kinetic reaction performance of Fe-NCNT catalyst is higher than rFe-NCNT and NCNT. The electron transfers number on Fe-NCNT, rFe-NCNT and NCNT were calculated using the Koutecky–Levich equation by plotting J^{-1} *versus* $\omega^{-1/2}$. The excellent linearity revealed the reduction of sulfur molecules in the electrolyte occurred at first order reaction kinetics. (Fig. 4e). The electron transfers number for Fe-NCNT, rFe-NCNT and NCNT catalysts are 7.3, 6.2 and 5.9, respectively, as exhibited in Fig. 4f. The higher electron transfer number of Fe-NCNT suggests an overall 8-electron reduction process with a possible conversion of S_8 into ${S_8}^{2-}$, implies that the synergistic of Fe-As and Fe-NPs in Fe-NCNT can effectively accelerate sulfur reduction.

In summary, we designed composite architecture with Fe-As and Fe-NPs co-embedded within N-doped carbon nanotube as a catalyst for high-performance of Li-S batteries. The homogeneous dispersed of Fe-As on Fe-NPs not only increased the chemisorption of polysulfides, but also enhanced the redox reaction kinetics. In addition, the interpenetrated nitrogen-doped in the lattice of carbon nanotubes as the sulfur host also enhanced the electrical conductivity of cathode. Therefore, the Fe-NCNT/S composite demonstrated a high initial specific capacity of 1502.6 mAh/g and reversible capacity of 597.8 mAh/g after 500 cycles at 1 C, with capacity decay as small as 0.069% per cycle. Moreover, the Fe-NCNT/S electrode with mass sulfur loading of 2.3 mg/cm^2 also shows a high reversible capacity of 610.6 mAh/g at 0.5 C after 200 cycles. Therefore, our work provided a new strategy to prepare an atom-nanoparticles dual-electrocatalyst combining strong chemisorption and accelerating polysulfide conversion for high-performance Li-S batteries.

Declaration of competing interest

The authors declare that they have no known competing financial interests or personal relationships that could have appeared to influence the work reported in this paper.

Acknowledgments

This work was supported by the Natural Science Foundation of China (Nos. 22125902, U2032202, 21975243 and 21825302), the National Program for Support of Topnotch Young Professionals, the Fundamental Research Funds for the Central Universities (No. WK2030020032), the DNL cooperation Fund, CAS (No. DNL202020) and the Anhui Science Fund for Distinguished Young Scholars (No. 2208085J15).

Supplementary materials

Supplementary material associated with this article can be found, in the online version, at doi:10.1016/j.cclet.2023.108190.

References

[1] S. Zhuang, Y. Kang, M. Liu, et al., J. Mater. Chem. A 9 (2021) 18927–18946.
[2] L. Matthew, L. Jun, K. Amine, ACS Nano 15 (2021) 8087–8094.
[3] T.Z. Hou, X. Chen, H.J. Peng, et al., Small 12 (2016) 3283–3291.
[4] A. Manthiram, Y. Fu, Y.S. Su, Acc. Chem. Res. 46 (2013) 1125–1134.
[5] N. Xu, T. Qian, X. Liu, et al., Nano Lett. 17 (2017) 538–543.
[6] L. Fan, M. Li, X. Li, et al., Joule 3 (2019) 361–386.
[7] J. Yan, X. Liu, B. Li, Adv. Sci. 3 (2016) 1600101.
[8] M. Li, R. Carter, A. Douglas, L. Oakes, C.L. Pint, ACS Nano 11 (2017) 4877–4884.
[9] R. Ummethala, M. Fritzsche, T. Jaumann, et al., Energy Stor. Mater. 10 (2018) 206–215.
[10] D. Su, C. Michael, G. Wang, Adv. Energy Mater. 7 (2017) 1602014.
[11] Y. Yang, C. Chen, J. Hu, et al., Chin. Chem. Lett. 29 (2018) 1777–1780.
[12] J. Cheng, Y. Liu, X.Zhang Y, et al., J. Chem. Eng. 419 (2021) 129649.
[13] F. Wu, E. Zhao, D. Gordon, et al., Adv. Mater. 28 (2016) 6365–6371.
[14] X. Sun, S. Liu, W. Sun, et al., Chin. Chem. Lett. 34 (2023) 107501.
[15] S. Yao, H. Tang, M. Liu, et al., J. Alloys Compd. 788 (2019) 639–648.
[16] J. Wu, Y. Dai, Z. Pan, et al., Appl. Surf. Sci. 510 (2020) 145529.
[17] C. Zhao, C. Shen, F. Xin, Z. Sun, W. Han, Mater. Lett. 137 (2014) 52–55.
[18] Z. Sun, J. Zhang, L. Yin, et al., Nat. Commun. 8 (2017) 1–8.
[19] W. Chen, H. Jin, S. Xie, et al., J. Energy Chem. 54 (2021) 16–22.
[20] L. Zhang, X. Chen, F. Wan, et al., ACS Nano 12 (2018) 9578–9586.
[21] M. Luo, Y. Bai, R. Sun, et al., J. Energy Chem. 73 (2022) 407–415.
[22] S. Yao, C. Zhang, R. Guo, et al., ACS Sustain. Chem. Eng. 8 (2020) 13600–13609.
[23] Z. Shen, X. Jin, J. Tian, et al., Nat. Catal. 5 (2022) 555–563.
[24] Z.C. Yue, G.W. Sun, Y.F. Bai, et al., J. Mater. Chem. 8 (2020) 18358–18366.
[25] Z. Qiao, F. Zhou, Q. Zhang, et al., Energy Stor. Mater. 23 (2019) 62–71.
[26] P. Zeng, C. Liu, X. Zhao, et al., ACS Nano 14 (2020) 11558–11569.
[27] Z. Liu, L. Zhou, Q. Ge, et al., ACS Appl. Mater. Interfaces 10 (2018) 19311–19317.
[28] C. Lu, Y. Chen, Y. Yang, X. Chen, Nano Lett. 20 (2020) 5522–5530.
[29] Y. Miao, Y. Zheng, F. Tao, et al., Chin. Chem. Lett. 34 (2023) 107121.
[30] Z. Du, X. Chen, W. Hu, et al., J. Am. Chem. Soc. 141 (2019) 3977–3985.
[31] Z. Liu, L. Zhou, Q. Ge, et al., ACS Appl. Mater. Interfaces 10 (2018) 19311–19317.
[32] H. Tian, A. Song, H. Tian, et al., Chem. Sci. 12 (2021) 7656–7676.
[33] C.C. Hou, L. Zou, Q. Xu, Adv. Mater. 31 (2019) 1904689.
[34] Z.H. Luo, M. Feng, H. Lu, et al., Ind. Eng. Chem. Res. 58 (2019) 1812–1822.
[35] C.C. Hou, L. Zou, Q. Xu, Adv. Mater. 31 (2019) 1904689.
[36] G. Li, J. Zhang, W. Li, et al., Nanoscale 10 (2018) 9252–9260.
[37] Z. Liu, L. Wang, W. Yang, Chin. Chem. Lett. 32 (2021) 2919–2922.
[38] L. Hong, K. Du, C. Xiang, et al., J. Mater. Chem. A 8 (2020) 17136–17149.
[39] H. Nie, M. Li, Q. Li, et al., Chem. Mater. 26 (2014) 3104–3112.